Effect of Spatial Filtering in Implicit Large-Eddy Simulations of Separated Flows

Ali Uzun*

National Institute of Aerospace, Hampton, Virginia 23666

and

Mujeeb R. Malik[†]

NASA Langley Research Center, Hampton, Virginia 23681

Nomenclature

a_n	=	spatial filter coefficient at stencil point n
C	=	logarithmic layer intercept constant
C_f	=	skin-friction coefficient
C_p	=	pressure coefficient
c	=	chord length
f	=	unfiltered quantity
$\bar{f}$	=	filtered quantity
K	=	turbulent kinetic energy
N	=	spatial filter stencil width parameter
n	=	spatial filter stencil point index
p	=	pressure
Re_c	=	chord-based Reynolds number; $\rho_\infty u_\infty c / \mu_\infty$
r	=	radial direction
r_{wall}	=	wall radius
U	=	mean axial velocity component
u	=	axial velocity component
u_i	=	velocity component in Cartesian coordinate system
u_τ	=	friction velocity
v	=	radial velocity component
x	=	axial direction
x_j	=	Cartesian coordinate system
α_f	=	filtering parameter
Δt	=	computational time step
ε_n	=	numerical dissipation of turbulent kinetic energy
ε_p	=	physical dissipation of turbulent kinetic energy
κ	=	von Kármán constant
μ	=	molecular viscosity
ν	=	kinematic viscosity; μ/ρ
ρ	=	fluid density
$\bar{\rho}$	=	mean fluid density
σ_{ji}	=	fluctuating viscous stress tensor
τ_{wall}	=	wall shear stress
$\langle \rangle$	=	temporal and/or azimuthal averaging operator
∇	=	gradient operator

Subscripts

i	=	value at grid point i; velocity component in Cartesian coordinate system
j	=	Cartesian coordinate system index
w	=	distance from wall
∞	=	freestream value

Superscripts

a	=	after filter application
b	=	before filter application
$\prime$	=	perturbation from mean value
$\prime\prime$	=	Favré fluctuation
$+$	=	value given in wall units

I. Introduction

THE relatively high Reynolds number of turbulent flows encountered in various applications puts these problems well beyond the reach of direct numerical simulation (DNS) at present. Meanwhile, lower-fidelity Reynolds-averaged Navier–Stokes (RANS) calculations are known to be not accurate enough in complex problems, such as smooth-body flow separation and other flows involving highly unsteady phenomena. Hence, given the current infeasibility of DNS and the unsatisfactory performance of RANS, intermediate techniques such as large-eddy simulation (LES) and hybrid RANS–LES, for which the fidelity lies between RANS and DNS, have received much attention for application to various problems of practical importance.

Modeling of the effect of missing scales on resolved scales, also known as subgrid-scale (SGS) modeling, is an important subject for LES. SGS models can be broadly categorized as explicit or implicit approaches. The explicit approach is based on an SGS model that explicitly appears in the governing equations expressed in the form of so-called "filtered Navier–Stokes equations," which describe the evolution of the turbulence scales resolved by the LES grid. The effect of the scales unresolved by the grid is represented by the SGS model. The implicit modeling approach, on the other hand, does not employ an explicit model but instead treats the intrinsic dissipation of the numerical discretization scheme as an implicit SGS model. An LES without an explicit SGS model is commonly termed as an implicit LES (ILES). The relative merits of one SGS modeling approach over another is a subject of ongoing debate.

We have opted to employ an ILES methodology, based on high-order compact finite difference and spatial filtering schemes, in our recent investigations of separated flow problems [1,2]. Further discussion of our preference of ILES over explicit LES was provided by Uzun and Malik [2]. The ILES methodology adopted in our work is very similar to that originally devised by Visbal and Rizetta [3] and Visbal et al. [4]. The spatial filtering operation, described in the next section, is treated as an implicit SGS model for the ILES. Some observations made during the course of our recent investigations, which pointed out excessive numerical dissipation in certain parts of the flowfield, prompted us to take a closer look at the potential effect of the spatial filter on ILES predictions. This technical Note is therefore devoted to spatial filter effects in the context of a high-Reynolds-number transonic shock-induced separated flow.
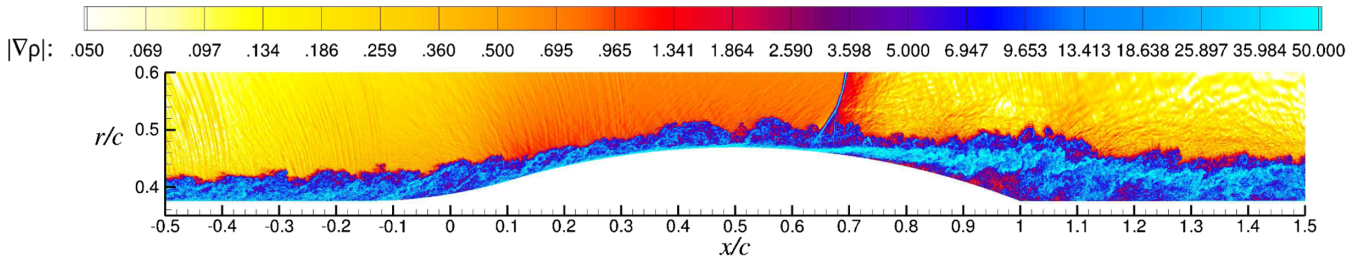
II. Spatial Filter Formulation

Details of the simulation methodology can be found in our recent publications [1,2]. The spatial filter [5,6] employed in our methodology is given by the following expression:

Fig. 1 Numerical schlieren (depicted in terms of normalized density gradient magnitude) visualizing shock-induced flow separation in Bachalo–Johnson flow.

$$\alpha_f \bar{f}_{i-1} + \bar{f}_i + \alpha_f \bar{f}_{i+1} = \sum_{n=0}^{N} \frac{a_n}{2} (f_{i+n} + f_{i-n}) \qquad (1)$$

where $\bar{f}_i$ denotes the filtered value of quantity f at grid point i; α_f is the filtering parameter in the range $-0.5 < \alpha_f \leq 0.5$; and $N = 3, 4$, and 5 for the sixth-, eighth-, and tenth-order filters, respectively. A less dissipative filter is obtained as α_f is varied toward its upper limit. The coefficients a_n depend on N and α_f. The preceding expression is valid for the interior grid points away from the boundaries. In the vicinity of the boundaries, one-sided biased schemes that preserve the original order of accuracy of the interior formulation are used [5] in the present study. To further enhance robustness and numerical stability, lower-order one-sided biased formulations that step up the order of the accuracy toward the interior may also be applied. Although such a strategy is not explored here, it could prove particularly useful in problems involving more complex curvilinear grids with less than optimal near-wall grid spacings. The boundary points are left unfiltered in the present work. The filter is applied sequentially along each of the three spatial directions. The solution, represented in the form of conserved flow variables, is normally filtered once after each subiteration of the implicit time advancement scheme [7].

As the filter order of accuracy is increased at a fixed α_f, the amount of numerical dissipation added by the spatial filter decreases. On relatively coarse grids, the combination of the optimized fourth-order compact finite difference scheme [8], which is used in our methodology, with the eighth- or tenth-order filters is usually unstable. In our experience, these higher-order filters generally require fairly high-resolution grids for numerical stability. The sixth-order filter, on the other hand, has shown robustness on a wide range of grids with varying resolutions used in past problems. Determining the minimal amount of numerical dissipation needed to keep the simulation stable on a given grid requires numerical experimentation with filters of varying orders of accuracy. This way, the highest-order filter that is stable on a given grid resolution can be identified. The filtering parameter can also be varied to control the dissipation; however, a significant deviation from $\alpha_f \approx 0.49$ would also lead to an excessive amount of numerical dissipation. In the present study, we keep $\alpha_f = 0.49$ while varying the filter order of accuracy.

III. Test Case: Transonic Shock-Induced Flow Separation

The test case of the present study involves the shock-induced boundary-layer separation over an axisymmetric bump mounted on a straight cylinder, which is representative of the upper surface of a transonic airfoil. Figure 1 depicts the main features of the problem of interest. This test case, also known as the Bachalo–Johnson flow [9], was simulated recently using up to 24 billion grid points [2]. The freestream Mach number is 0.875. The Reynolds number based on the chord length c and the freestream velocity u_∞ is $Re_c = 2.763$ million. In the present study, filtering is applied throughout the entire domain, including the shock-containing region. Additional adaptive artificial dissipation [10] is added in the shock vicinity. A shock sensor, similar to that proposed by Ducros et al. [11], identifies the shock-containing region to which adaptive artificial dissipation is applied. Without this additional artificial dissipation, filtering alone causes noticeable ringing across the shock. Such wiggles generated

around the shock, which will eventually lead to numerical instability if left untreated, are eliminated by the additional artificial dissipation added in that region. Further details of this test case and the experiment were given by Uzun and Malik [2].

A. Simulation Details

We consider a 120 deg slice of the axisymmetric body with periodic boundary conditions applied on the edges of the slice. The number of grid points is 24 billion. Two calculations are performed as an ILES that respectively, employs the sixth- and tenth-order filters as an implicit SGS model. The tenth-order filter results are averaged up to 15 chord flow times (based on freestream velocity), whereas the sixth-order filter results are averaged over 6.5 chord flow times. The sixth-order filter ILES was performed before the tenth-order filter ILES. Because of the very large grid point count and limited computational resources, it was not run as long as the tenth-order case once the intermediate results gathered during this simulation revealed evidence of excessive numerical dissipation added by the sixth-order filter. Nevertheless, the shorter time average of the sixth-order filter results is not expected to make a dramatic difference in the comparisons to be made between the two cases and does not detract from the main conclusions of this study. For the tenth-order filter case, the results averaged over 10 chord flow times are shown in this Note. The results averaged over 15 chord flow times can be found in the work of Uzun and Malik [2], wherein further computational details are also available.

B. Simulation Results

Figure 2 shows the pressure and skin-friction coefficient distributions from the two simulations and the comparison with the other data. The experimental surface pressure measurements were taken separately in a 2×2 ft transonic tunnel [9] and a 6×6 ft supersonic tunnel [12,13]. The small tunnel data are available from NASA Langley Research Center's Turbulence Modeling Resource database.[‡] Two sets of the large tunnel surface pressure data are extracted separately from the relevant figures given by Horstman and Johnson [12] and Johnson [13]. Besides the shock location difference between the two tunnel tests, some scatter in the postshock region pressure data is also present. No skin-friction measurements were taken in the experiment. The pressure and skin-friction coefficients are defined as

$$C_p = \frac{p - p_\infty}{(1/2)\rho_\infty u_\infty^2} \quad \text{and} \quad C_f = \frac{\tau_{\text{wall}}}{(1/2)\rho_\infty u_\infty^2} \qquad (2)$$

where ρ and p, respectively, are the density and pressure; τ_{wall} is the wall shear stress; and the subscript ∞ denotes the reference freestream conditions.

The present simulations do not model the tunnel wall effects and use characteristic freestream boundary conditions at the outer boundary that are more likely to replicate the large tunnel results. As seen in Fig. 2a, relative to the sixth-order filter result, the tenth-order filter ILES predicts the shock position in slightly better agreement with the large tunnel data. This is one potential indicator of the

‡Data available online at https://turbmodels.larc.nasa.gov [retrieved 5 August 2019].
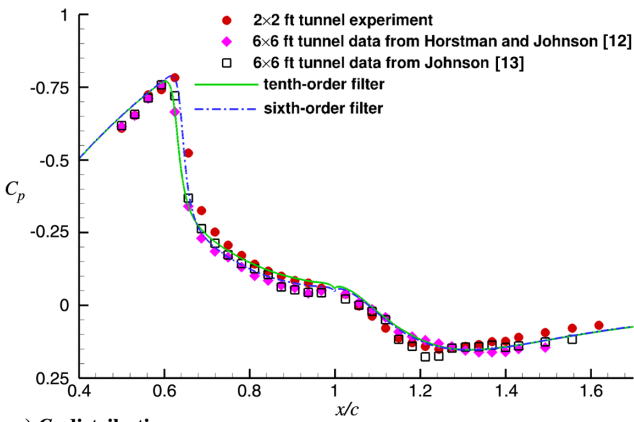
a) C_p distributions
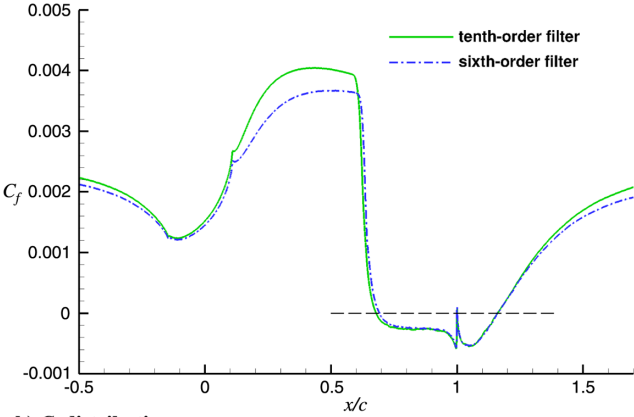
b) C_f distributions

Fig. 2 Effect of filter order of accuracy on C_p and C_f.

improved solution accuracy obtained with the tenth-order filter. Some variation in the postshock region C_p predictions between the two cases is also evident in the figure. The two ILES predictions are nearly identical downstream of the trailing edge. Figure 2b shows important differences in the C_f predictions with the two cases. The peak C_f value observed upstream of separation is nearly 10% higher with the tenth-order filter. This shows that the sixth-order filter has a considerable impact on the attached flow behavior near the wall in the accelerating region upstream of flow separation. Because of the upstream shift in the shock position, the tenth-order filter result shows slightly earlier separation relative to the sixth-order case. The separation point is predicted at $x/c \approx 0.69$ and 0.68 by the sixth- and tenth-order filter simulations, respectively. These agree well with the corresponding observation made in the large tunnel experiment, which showed the separation in the vicinity of $x/c \approx 0.66$–0.69. Both cases predict a nearly identical reattachment location, at $x/c \approx 1.16$, which is fairly close to the value of 1.17 observed in the large tunnel experiment.

The significant difference in the peak C_f region predictions between the two cases also leads to some differences in the near-wall grid resolution in terms of wall units. Table 1 compares the streamwise, radial, and azimuthal spacings in wall units in the region

where $0.2 \leq x/c \leq 0.5$. The higher skin-friction level computed with the tenth-order filter in the peak region naturally leads to larger grid spacings in wall units. In that region, the differences in wall unit spacings between the two cases vary from about 5 to 7%.

Figures 3 and 4 show the effect of the filter on the mean velocity and Reynolds stress profiles, respectively. In these figures, r_w/c denotes the radial distance measured from the wall normalized by the chord; u and v are the axial and radial velocity components, respectively; and the $\langle \rangle$ operator denotes averaging in time and along the azimuthal span. The superscript $\prime$ on u or v denotes the velocity fluctuation. These predictions are compared with corresponding experimental measurements, which are only available from the small tunnel experiment [9]. The first axial station is located upstream of the bump leading edge, at $x/c = -0.25$; whereas the remaining ones are located within the separation bubble and the reattachment region. The predicted mean velocity profiles, depicted in Fig. 3, are generally similar between the two cases, with only some modest differences. As will be seen, the main effect of the filter on the mean velocity profiles is felt in the logarithmic layer behavior near the wall in the attached flow region. The velocity profile predictions at $x/c = -0.25$, which is located in the attached region well upstream of separation, show reasonable agreement with the experiment. As discussed by Uzun and Malik [2], because of the wall interference effects in the small tunnel experiment, the separated shear layer in the experiment reattaches considerably earlier relative to the simulations, at around $x/c \approx 1.1$. The simulations predict a delayed reattachment due to the missing wall interference effects. Nevertheless, the velocity profile comparisons within the separation bubble (where $x/c = 0.813$, 0.938, and 1) display reasonable similarity to the experiment. Because of the delayed reattachment in the calculations relative to the small tunnel experiment, the comparisons in the vicinity of the experimental reattachment location and downstream show greater differences relative to the experiment, as can be seen at $x/c = 1.125$ and 1.25.

Reynolds stress comparisons, shown in Fig. 4, reveal significant differences between the two cases. The tenth-order filter ILES predicts generally higher peak Reynolds stress levels relative to the sixth-order filter ILES at all stations. This suggests that the sixth-order filter is generally more dissipative than the tenth-order filter on the present grid. The Reynolds stress comparisons depict generally similar qualitative behaviors between the simulations and the experiment, but there are noticeable differences in the peak values at some stations. The earlier flow reattachment in the small tunnel experiment suggests a faster growth of the separated shear layer relative to that in the simulations. The higher Reynolds stress levels observed in much of the separated region in the experiment would correlate well with the faster shear layer growth. Further discussion of the Reynolds stresses can be found in the work of Uzun and Malik [2].

Figure 5a shows the mean axial velocity profiles in wall units at the bump apex (i.e., at $x/c = 0.5$) obtained in the two cases. In this figure, $r_w^+ = r_w u_\tau/\nu$, $U^+ = U/u_\tau$, $r_w = r - r_{\text{wall}}$ is the radial wall distance (which is the same as the wall-normal distance because the radial direction is aligned with the wall-normal direction at the bump apex); U is the mean axial velocity; $u_\tau = \sqrt{\tau_{\text{wall}}/\rho}$ is the friction velocity; τ_{wall} is the wall shear stress; and ρ and ν, respectively, are the density and kinematic viscosity on the wall. Even though the turbulent boundary layer is in an accelerated flow regime at this location, the tenth-order filter ILES profile appears to possess a

Table 1 Near-wall grid spacings in wall units at several streamwise locations

Streamwise location	Streamwise spacing	Radial spacing	Azimuthal spacing
$x/c = 0.2$, sixth-order filter	27.5	0.88	15.6
$x/c = 0.2$, tenth-order filter	29.6	0.95	16.8
$x/c = 0.3$, sixth-order filter	27.8	0.89	16.5
$x/c = 0.3$, tenth-order filter	29.8	0.95	17.6
$x/c = 0.4$, sixth-order filter	27.1	0.87	16.4
$x/c = 0.4$, tenth-order filter	28.6	0.92	17.4
$x/c = 0.5$, sixth-order filter	25.9	0.83	15.8
$x/c = 0.5$, tenth-order filter	27.2	0.87	16.6

a) *x/c* = −0.25

b) *x/c* = 0.813

c) *x/c* = 0.938
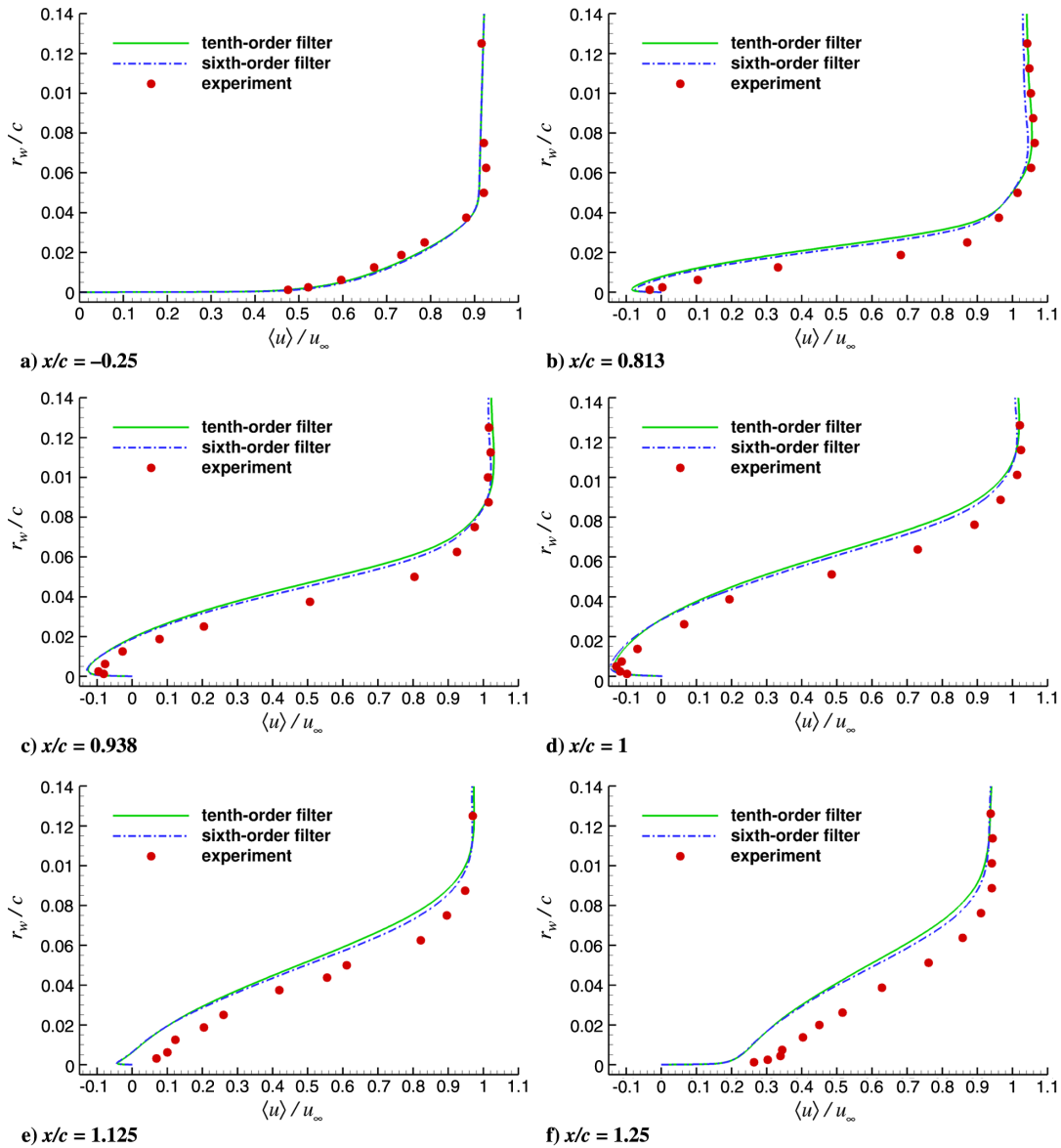
d) *x/c* = 1

e) *x/c* = 1.125

f) *x/c* = 1.25

Fig. 3   Effect of filter order of accuracy on the mean axial velocity profiles.

well-defined logarithmic layer, for which the constants (von Kármán constant of $\kappa = 0.4$ and an intercept constant of $C = 5.2$) agree with the typical values valid for zero-pressure-gradient boundary layers. The logarithmic layer is defined as $U^+ = \kappa^{-1} \ell_n (r_w^+) + C$. The sixth-order filter ILES mean velocity profile displays a shift above the logarithmic layer by as much as 1.5 units.

To investigate the reason for the different logarithmic layer behavior observed with the sixth-order filter, Fig. 5b plots the physical dissipation of turbulent kinetic energy (TKE) at $x/c = 0.5$ and compares it with the numerical dissipation of the filtering operation with varying orders of accuracy. The profiles are nondimensionalized using the bump chord length, ambient sound speed, and freestream kinematic viscosity. The physical dissipation is computed from the dissipation term in the Favré-averaged TKE transport equation for compressible flow, which can be found in the work of Adumitroaie et al. [14]. In Cartesian coordinates, the physical dissipation is given by

$$\varepsilon_p = \frac{1}{\bar{\rho}} \langle \sigma_{ji} \partial u_i'' / \partial x_j \rangle \tag{3}$$

where $\bar{\rho}$ is the mean density, σ_{ji} is the fluctuating viscous stress tensor (computed using the velocity fluctuation field), u_i'' is the velocity fluctuation component, x_j is the spatial direction, and $\langle \rangle$ denotes

azimuthal averaging. An instantaneous snapshot of the flowfield, obtained from the simulation performed with the sixth-order filter, is used to compute the physical dissipation profiles at $x/c = 0.5$ for all azimuthal positions, which are then averaged to obtain the profile shown here.

To determine the amount of TKE removed by the filtering operation with varying orders of accuracy, the same instantaneous flow solution is filtered separately using the sixth-, eighth-, and tenth-order filters. The numerical dissipation of the respective filter is computed as $\varepsilon_n = (K^b - K^a)/\Delta t$, where K is the TKE; the superscripts b and a denote "before" and "after" the filter application, respectively; and Δt is the computational time step. The instantaneous numerical dissipation profiles at $x/c = 0.5$ are computed for all azimuthal positions and are averaged to obtain the profiles shown here. As expected, the physical dissipation peaks on the wall and naturally decays with the wall distance. The numerical dissipation of the sixth-order filter is found to be much higher than that of the tenth-order filter and becomes comparable to the physical dissipation for r_w^+ greater than 20 or so, which is precisely in the region where the deviation from the logarithmic layer occurs. The sixth-order filter therefore applies significantly more numerical dissipation than the tenth-order filter in the near-wall region, which further manifests its effects in the form of a lowered skin friction and an upward shift in the logarithmic layer of the mean velocity profile.
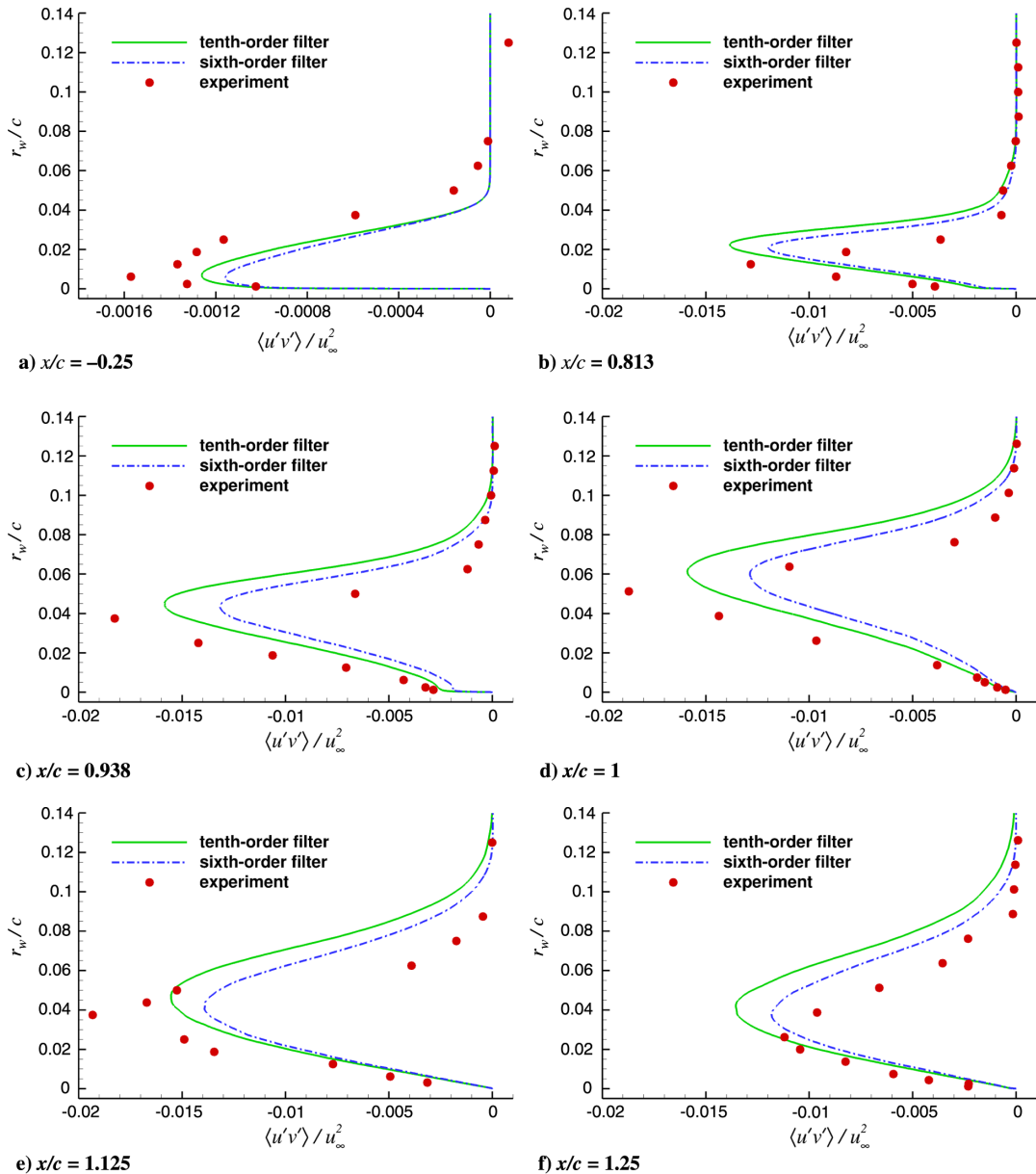
a) $x/c = -0.25$

b) $x/c = 0.813$

c) $x/c = 0.938$

d) $x/c = 1$

e) $x/c = 1.125$

f) $x/c = 1.25$

Fig. 4   Effect of filter order of accuracy on the Reynolds stress profiles.

A simulation with an eighth-order filter was not considered in this study, mainly because the simulation on the present grid was found to be stable with the tenth-order filter. As seen in Fig. 5b, the numerical dissipation profile of the eighth-order filter falls in between those of the other two filters. As the numerical dissipation of the tenth-order filter is enough to keep the simulation stable, the eighth-order filter would add more than enough dissipation if it were to be used in a simulation on the present grid. Hence, the results with the eighth-order filter would likely differ from those obtained with the tenth-order filter.

IV.   Conclusions

The effect of spatial filtering order of accuracy in ILES has been examined in a high-Reynolds-number transonic shock-induced separated flow. The tenth-order filter provides a minimal amount of numerical dissipation on the present grid, whereas the sixth-order filter yields a significant amount of numerical dissipation as compared to the physical turbulent dissipation. The predictions are negatively impacted by the excessive numerical dissipation of the sixth-order filter. The findings demonstrate that the numerical dissipation of the implicit SGS model can introduce detrimental effects that lead to erroneous predictions. It is therefore recommended to use

the highest-order filter that is stable on a given grid while keeping the filtering parameter as close as possible to its upper limit. In problems involving more complex curvilinear grids and geometries, rather than operating on or near the edge of numerical stability of the highest-order filter, one may opt to use a lower-order filter and add further grid resolution to limit the numerical dissipation. Such a strategy can help augment the robustness of the simulation methodology in particularly complex cases. Regardless of the strategy adopted for a given problem, grid resolution studies should also be performed whenever feasible in order to ensure reasonable numerical convergence of the results.

Finally, it is noted that the main conclusions in the present study concur with the earlier related findings of Visbal et al. [4]. In that study, the traditional fourth- and sixth-order compact finite difference schemes were coupled with the same Padé-type filters used here. Visbal et al. [4] concluded the following:

The filter must not introduce dissipation at the wavenumbers captured accurately by the baseline discretization while ensuring sufficient dissipation of high-frequency components in order to maintain long-term numerical stability. The use of fourth- and sixth-order interior Padé-filters in the
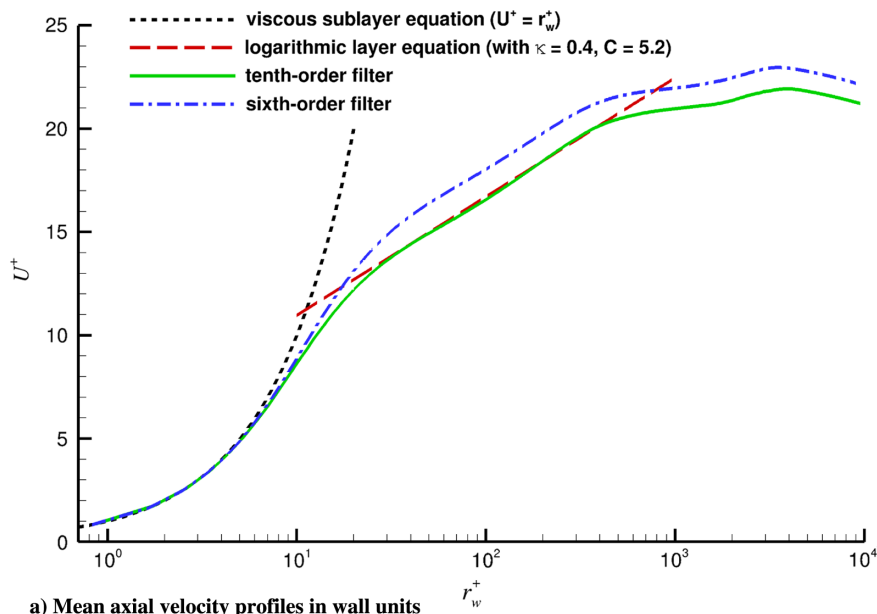
a) Mean axial velocity profiles in wall units
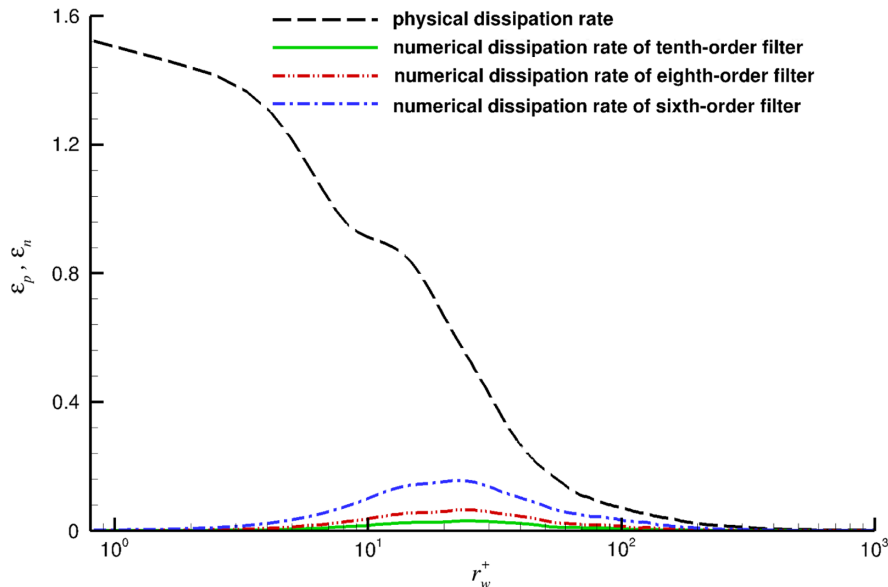
b) Comparison between physical and numerical dissipation profiles

Fig. 5 Mean axial velocity profiles and comparison between physical and numerical dissipations at $x/c = 0.5$.

homogeneous directions was found to be inadequate even when optimized for an improved spectral response.

The optimized prefactored fourth-order-accurate compact finite difference scheme [8] used in the present work is derived from the standard eighth-order compact scheme and has been shown to have better resolution in the high–wave-number range than the standard eighth-order compact scheme. The current analysis indicates that the eighth-order filter would add more dissipation than what is needed to keep the simulation stable on the present grid and provides further justification for the use of the tenth-order filter with minimal numerical dissipation. It is hoped that the knowledge gained in this study will contribute toward establishing the best practices for ILES based on spatial filtering.

Acknowledgments

References

[1] Uzun, A., and Malik, M. R., "Large-Eddy Simulation of Flow over a Wall-Mounted Hump with Separation and Reattachment," *AIAA Journal*, Vol. 56, No. 2, 2018, pp. 715–730.
doi:10.2514/1.J056397

[2] Uzun, A., and Malik, M. R., "Wall-Resolved Large-Eddy Simulations of Transonic Shock-Induced Flow Separation," *AIAA Journal*, Vol. 57, No. 5, 2019, pp. 1955–1972.
doi:10.2514/1.J057850

[3] Visbal, M. R., and Rizzetta, D. P., "Large-Eddy Simulation on Curvilinear Grids Using Compact Differencing and Filtering Schemes," *Journal of Fluids Engineering*, Vol. 124, No. 4, 2002, pp. 836–847.
doi:10.1115/1.1517564

[4] Visbal, M. R., Morgan, P. E., and Rizzetta, D. P., "An Implicit LES Approach Based on High-Order Compact Differencing and Filtering

Schemes," *16th AIAA Computational Fluid Dynamics Conference*, AIAA Paper 2003-4098, June 2003.
doi:10.2514/6.2003-4098

[5] Gaitonde, D. V., and Visbal, M. R., "Padé-Type Higher-Order Boundary Filters for the Navier–Stokes Equations," *AIAA Journal*, Vol. 38, No. 11, 2000, pp. 2103–2112.
doi:10.2514/2.872

[6] Visbal, M. R., and Gaitonde, D. V., "Very High-Order Spatially Implicit Schemes for Computational Acoustics on Curvilinear Meshes," *Journal of Computational Acoustics*, Vol. 9, No. 4, 2001, pp. 1259–1286.
doi:10.1142/S0218396X01000541

[7] Ekaterinaris, J. A., "Implicit, High-Resolution, Compact Schemes for Gas Dynamics and Aeroacoustics," *Journal of Computational Physics*, Vol. 156, No. 2, 1999, pp. 272–299.
doi:10.1006/jcph.1999.6360

[8] Ashcroft, G., and Zhang, X., "Optimized Prefactored Compact Schemes," *Journal of Computational Physics*, Vol. 190, No. 2, 2003, pp. 459–477.
doi:10.1016/S0021-9991(03)00293-6

[9] Bachalo, W. D., and Johnson, D. A., "Transonic, Turbulent Boundary-Layer Separation Generated on an Axisymmetric Flow Model," *AIAA Journal*, Vol. 24, No. 3, 1986, pp. 437–443.
doi:10.2514/3.9286

[10] Kim, J. W., and Lee, D. J., "Adaptive Nonlinear Artificial Dissipation Model for Computational Aeroacoustics," *AIAA Journal*, Vol. 39, No. 5, 2001, pp. 810–818.
doi:10.2514/2.1414

[11] Ducros, F., Ferrand, V., Nicoud, F., Weber, C., Darracq, D., Gacherieu, C., and Poinsot, T., "Large-Eddy Simulation of the Shock/Turbulence Interaction," *Journal of Computational Physics*, Vol. 152, No. 2, 1999, pp. 517–549.
doi:10.1006/jcph.1999.6238

[12] Horstman, C. C., and Johnson, D. A., "Prediction of Transonic Separated Flows," *AIAA Journal*, Vol. 22, No. 7, 1984, pp. 1001–1003.
doi:10.2514/3.48539

[13] Johnson, D. A., "Transonic Separated Flow Predictions with an Eddy-Viscosity/Reynolds-Stress Closure Model," *AIAA Journal*, Vol. 25, No. 2, 1987, pp. 252–259.
doi:10.2514/3.9615

[14] Adumitroaie, V., Ristorcelli, J. R., and Taulbee, D. B., "Progress in Favré-Reynolds Stress Closures for Compressible Flows," *Physics of Fluids*, Vol. 11, No. 9, 1999, pp. 2696–2719.
doi:10.1063/1.870130

J. Poggie
Associate Editor